Morphologic dating of fault scarps using airborne laser swath mapping (ALSM) data

G. E. Hilley,[1] S. DeLong,[2] C. Prentice,[2] K. Blisniuk,[3] and JR. Arrowsmith[4]

Received 8 December 2009; revised 6 January 2010; accepted 11 January 2010; published 18 February 2010.

[1] Models of fault scarp morphology have been previously used to infer the relative age of different fault scarps in a fault zone using labor-intensive ground surveying. We present a method for automatically extracting scarp morphologic ages within high-resolution digital topography. Scarp degradation is modeled as a diffusive mass transport process in the across-scarp direction. The second derivative of the modeled degraded fault scarp was normalized to yield the best-fitting (in a least-squared sense) scarp height at each point, and the signal-to-noise ratio identified those areas containing scarp-like topography. We applied this method to three areas along the San Andreas Fault and found correspondence between the mapped geometry of the fault and that extracted by our analysis. This suggests that the spatial distribution of scarp ages may be revealed by such an analysis, allowing the recent temporal development of a fault zone to be imaged along its length. **Citation:** Hilley, G. E., S. DeLong, C. Prentice, K. Blisniuk, and JR. Arrowsmith (2010), Morphologic dating of fault scarps using airborne laser swath mapping (ALSM) data, *Geophys. Res. Lett.*, *37*, L04301, doi:10.1029/2009GL042044.

1. Introduction

[2] Fault zones are complex, multistranded features that accommodate the cumulative deformation across the fault zone over thousands to millions of years. Fault scarps can be formed in fault zones, and their topographic form may indicate their relative activity [e.g., *Lawson and Reid*, 1908]. In some fault zone models, strain softening of the fault surface may lead to strain localization along a single failure surface over time, while hardening may lead to the progressive abandonment and initiation of many individual fault strands [e.g., *Scholz*, 1988]. At least over the last several hundred to several tens-of-thousands of years, this record of past fault strand activity may be revealed by the topography of the fault zone, and where relative ages of scarps can be inferred, the temporal development of the fault zone may be revealed by topographic analysis.

[3] Geologists have recognized that a fault scarp, once formed and subject to an initial period of rapid degradation, degrades in close analogy to the temperature profile expected from heat conduction [e.g., *Hanks et al.*, 1984]. The idea that hillslope processes such as bioturbation, rainsplash, and soil creep transport mass in a diffusive manner has been recognized since the early 1900s [*Davis*, 1892; *Gilbert*, 1909]; however, it was not until much later that quantitative estimates of fault scarp ages were inferred from their topographic form in areas where mass transport rates could be calibrated with absolute age dating methods under the assumption of diffusive transport [e.g., *Hanks*, 2000, and references therein]. In these studies, topographic surveys conducted along profiles across scarps were commonly carried out by theodolite surveying [e.g., *Hanks*, 2000]. This restricted such morphologic scarp dating to limited areas where scarps could be clearly identified and painstakingly surveyed.

[4] In 2005–2008, the National Center for Airborne Laser Mapping collected high resolution digital topography along the entire length of the San Andreas Fault (SAF) in California. Because these data sample at least several ground elevations per square meter, they can be used to create a high-resolution digital elevation model (DEM) of the narrow (~1–4 km-wide) swath along the fault zone. The high resolution of ground points also allows the bare-earth surface to be extracted. Analysis of such a dataset has the potential to reveal the temporal development of fault strands within the zone over the last several tens-of-thousands of years, how this development may change along the length of the fault zone, and may reveal previously unknown and unmapped strands of the fault. This contribution presents a method for identifying scarp-like features within the high resolution topographic swaths, extracting their morphologic ages, and finding the orientation of these features.

2. Methods

[5] Our analysis uses similarity between a particular morphologic feature and high-resolution topographic data to extract the location of these features [e.g., *Gallant and Hutchinson*, 1997]. To do this, a scarp-like template is lagged over the digital topography to highlight areas where the topography conforms to the scarp's morphology. The template must have zero mean and sufficiently rapid decay to provide localization in space, such that the redundancy in the identified location of template-like forms in the topography is minimized. In this approach we use an analytical expression for the expected temporal degradation of a scarp as our template, because there is a rationale for modeling mass transport across scarps according to a diffusive process when slopes are low [e.g., *Gilbert*, 1909; *Andrews and Bucknam*, 1987]. The solution for the temporal evolution of the topographic

[1]Department of Geological and Environmental Sciences, Stanford University, Stanford, California, USA.
[2]U.S. Geological Survey, Menlo Park, California, USA.
[3]Department of Geology, University of California, Davis, California, USA.
[4]School of Earth and Space Exploration, Arizona State University, Tempe, Arizona, USA.

0094-8276/10/2009GL042044$05.00

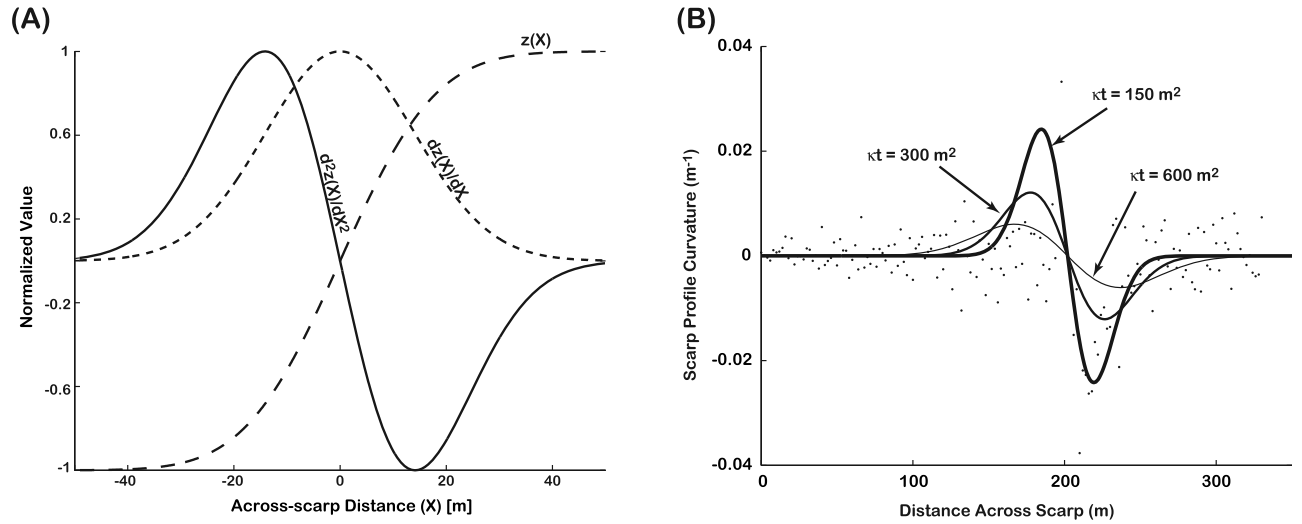

Figure 1. (a) Across-scarp profile showing $z(X)$, $dz(X)/dX$, and d^2z/dx^2 for $\kappa t = 10$ m^2. (b) Across-scarp curvature calculated from ALSM data (points) along a 40-m-long scarp in the Carrizo Plain whose location is denoted in Figure 2. This scarp's height is ~15 m and its morphologic age was calculated to be ~150–170 m^2 based on ground surveying and analysis reported by *Arrowsmith et al.* [1998]. Theoretical profiles resulting from κt values of 150 m^2, 300 m^2, and 600 m^2 are shown as solid lines.

profile of an infinitely long fault scarp that evolves according to a diffusion equation is (Figure 1):

$$z(X) = a\ \mathrm{erf}\left(\frac{X}{2\sqrt{\kappa t}}\right) + bX \tag{1}$$

where $z(X)$ is the scarp profile elevation, X is the across-scarp distance, t is the time since the scarp was formed, a is half of the initial scarp height, b is the far-field slope, and κ is a rate constant that encapsulates the voracity of mass transport processes across the scarp. Because κt always occur together in equation (1), this product is often referred to as the "morphologic age" of the scarp that provides a quantitative estimate of relative scarp ages. This formulation for the scarp profile evolution assumes that a discontinuous vertical offset of $2a$ was produced at $t = 0$ and that the offset is maintained at all times at $X \rightarrow -\infty$ and $X \rightarrow \infty$.

[6] Equation (1) does not decay to zero as $|X|$ increases, and so will not localize when convolved with the surface. In addition, the scarp evolution described by equation (1) may be sensitive to the initial scarp angle that results from rapid mass failure processes that dominate mass transport across the scarp shortly following offset [e.g., *Hanks and Andrews*, 1989]. To provide this localization and reduce the dependence of the predicted scarp form on the initial scarp angle and far-field fan slope (see Text S1 of the auxiliary material), we use the second derivative of equation (1) as our template (Figure 1)[1]:

$$\frac{\partial^2 z}{\partial X^2} = \frac{-aX}{2\kappa t\sqrt{\pi\kappa t}}\exp\left(-\frac{X^2}{4\kappa t}\right) \tag{2}$$

[7] A two-dimensional template is constructed from equation (2) as follows. First, we compute $\partial^2 z/\partial X^2$, which represents the curvature of the surface in the across-scarp direction and replicate this curvature in the out-of-plane (Y) direction such that

$$\left[\frac{\partial^2 z}{\partial X^2}\right]_{template} = \begin{cases} \frac{-aX}{2\kappa t\sqrt{\pi\kappa t}}\exp\left(-\frac{X^2}{4\kappa t}\right) & \text{if } |Y| \le d \\ 0 & \text{otherwise} \end{cases} \tag{3}$$

where d is the along-strike length of the scarp (set equal to 200 m in the remainder of this analysis to represent a scarp-like feature that is elongated for distances along-strike that are typically greater than other features such as fluvial scarps). This two-dimensional template is then rotated such that the Y direction is oriented at a prescribed azimuthal angle (α) relative to north to model differently oriented fault scarps. As shown in Text S2, if this template is normalized such that

$$W(X,Y) = \frac{\left[\frac{\partial^2 z}{\partial X^2}\right]_{template}}{\int_{-\infty}^{\infty}\int_{-\infty}^{\infty}\left[\frac{\partial^2 z}{\partial X^2}\right]_{template} dXdY} \tag{4}$$

The convolution of equation (4) with the curvature of the surface in the across-scarp direction yields the least-squares best-fitting solution for a at each point in the digital topography.

[8] The curvature of the surface in the across-scarp direction is computed from the high-resolution digital topography using a second-order finite-difference approximation as follows:

$$\left[\frac{\partial^2 z}{\partial X^2}\right]_{surface} = \frac{\partial^2 z}{\partial x^2}\cos^2\alpha - 2\frac{\partial^2 z}{\partial x\partial y}\cos\alpha\sin\alpha + \frac{\partial^2 z}{\partial y^2}\sin^2\alpha \tag{5}$$

where x and y are the easting and northing locations of each point in the digital topography, respectively. By convolving the surfaces described by equations (4) and (5), we find the

[1] Auxillary materials are available in the HTML. doi:10.1029/2009GL042044.

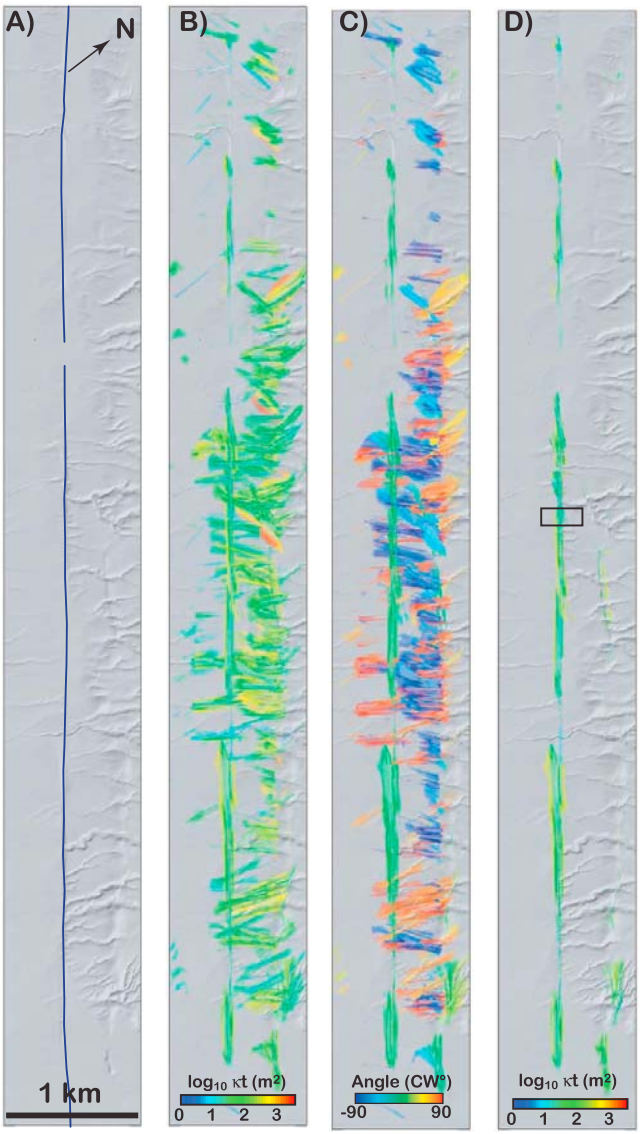

Figure 2. Results for analysis of topographic swath from the Carrizo Plain. (a) Shaded relief map, (b) best-fitting value of κt for all best-fit orientations of the scarp, (c) best-fitting scarp orientation, and (d) best-fitting value of κt for points whose best-fitting orientation deviates ±20° from the overall trend of the fault zone. In Figures 2b–2d, the transparency of the colors is scaled to the value of the SNR, with opaque colors showing values of SNR greater than two standard deviations from the mean SNR value, and transparent colors showing values of SNR less than two standard deviations below the mean SNR value. SNR values $\pm 2\sigma$ from the mean SNR value are variably transparent. Fault traces taken from *Vedder and Wallace* [1970]. Black frame in Figure 2d denotes location of curvature profile shown in Figure 1b.

best-fitting scarp amplitude at each point in the digital topography. Furthermore, we compute the signal to noise (SNR) ratio as the ratio of the squared scarp amplitudes to the sum of the squares of the misfit between the scarp with the best-fitting amplitude and the digital topography for each point in the digital elevation model. As shown in Text S2, the SNR can be computed as follows:

$$SNR = \frac{A^2}{E^2}$$

where

$$A = \left(\left[\frac{\partial^2 z}{\partial X^2} \right]_{surface} * W \right)$$

$$E^2 \times n = A^2 \int_{-\infty}^{\infty} \int_{-\infty}^{\infty} \left[\frac{\partial^2 z}{\partial X^2} \right]^2_{template} dx_1 dy_1 - 2A \left(\left[\frac{\partial^2 z}{\partial X^2} \right]_{surface} * \left[\frac{\partial^2 z}{\partial X^2} \right]_{template} \right) + \left(\left[\frac{\partial^2 z}{\partial X^2} \right]_{surface} * M \right)^2 \quad (6)$$

where "*" is the convolution operator, M is a masking matrix whose values are one if $W \neq 0$ and zero otherwise, and n is the number of non-zero values of M. Thus, for a prescribed scarp template orientation, along-strike length, and κt value that describes the relative age of the scarp, we use the Fast Fourier Transform (FFT) with the fact that $A * B$ is equivalent to $\mathcal{F}^{-1}\{\mathcal{F}\{A\} \cdot \mathcal{F}\{B\}\}$ to find the best-fitting scarp amplitude and SNR at each point in the DEM. To further determine the best-fitting scarp orientation and morphologic age at each point in the digital topography, we fix the along-strike scarp length to a constant value, and systematically vary the scarp orientation and morphologic age. Finally, the highest SNR value is used to identify the best-fitting scarp orientation, morphologic age, and scarp height for each point in the DEM.

3. Results

[9] We assessed the fidelity of this method using a synthetic scarp topography generated using equation (1). The synthetic scarp was chosen to strike N–S, with positive vertical motion on its W side. The total scarp offset was 5 m. Scarp elevations were computed every square meter over a 200 × 800 pixel grid and spatially incoherent noise with zero mean and a standard deviation of 0.1 m was superposed onto the synthetic scarp elevations. This produced a standard deviation of 0.11 m^{-1} of noise in the curvature values that were ultimately used to identify the best-fitting scarp form. The derived curvature noise should be regarded as conservative, for while landscape morphology deviates from idealized model forms by decimeters, this variation typically occurs over the distance of several meters. This longer length-scale reduces the noise when mapping these elevation changes into curvature. Synthetic data results for the morphologic age κt = 100 m^2 (Text S3 and Figures S2a–S2d) and κt = 1000 m^2 (Figures S2e–S2h) generally show that the recovery of the location, orientation, and κt of the scarp appears robust to noise levels typical of those that might be expected in natural examples. Scarps typified by larger κt values show longer-wavelength characteristics than their smaller κt counterparts, and so the lower curvature of these features makes them more susceptible to noise. In

Figure 3. Results for analysis of topographic swath from Mustang Ridge. (a–d) Plots are identical to those described in Figure 2, excepting that in Figure 3d, orientations that deviate ±40° from the overall trend of the fault zone were considered to capture the oblique structures that accommodate extension across the stepover. Surface fault traces modified from *Rymer et al.* [1984].

addition, the localization of the scarp identified by the template decreases with increasing κt due to the larger spatial scale of these template waveforms. In many active fault zones, the approximate orientation of the fault strand can be identified *a priori*, and so filtering best-fit κt and α values for a range of α that is within ±20° about the assumed trend of the fault zone (Figures S2d and S2h) further reduces noise in the analysis.

[10] This analysis was applied to three locations along the SAF with varying fault geometric complexities (locations shown in Figure S7) where 2-m-resolution bare-earth DEMs were constructed from the ALSM swath data. The first site is located in the Carrizo Plain, where the SAF has a simple, single-stranded fault geometry (Figure 2). The automated scarp extraction algorithm, when filtered for a range of scarp trends that deviate no more than 20° from the trend of the fault zone (Figure 2d), recovers the location of the fault zone. Also, morphologic ages of ~150–600 m^2 calibrated using ground surveying in the area [*Arrowsmith et al.*, 1998] agree well with those extracted by our analysis at identical locations. Features trending normal to the fault trend correspond with the margins of channels that cross the fault (Figure 2c), suggesting that our method may improperly identify such features as fault scarps when their trend is close to that of the overall trend of the fault zone. Further north along the SAF, an extensional stepover in the vicinity of Mustang Ridge causes deformation to be transferred between the main traces of the SAF by a series of N–S-striking normal faults [e.g., *Rymer et al.*, 1984]. In this case, we considered fault scarps that deviate from the overall trend of the SAF

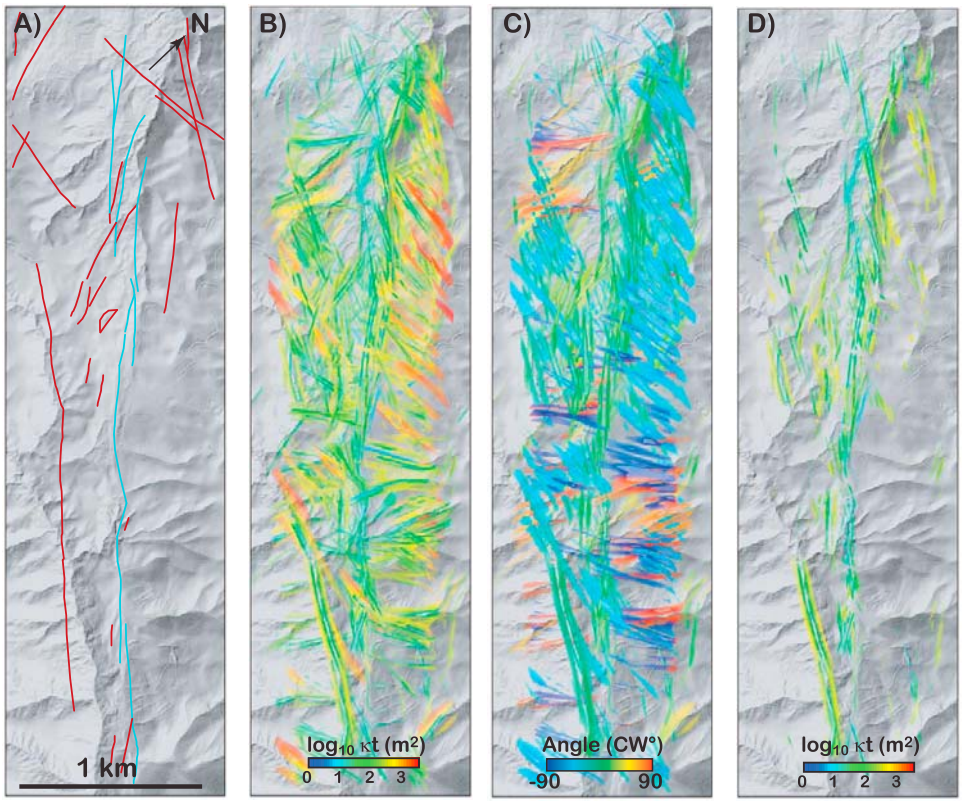

Figure 4. Results for analysis of topographic swath from Mustang Ridge. (a–d) Plots are identical to those described in Figure 2. Surface fault traces taken from *Sarna-Wojcicki et al.* [1975]. Blue lines in figure denote approximate location of the surface rupture trace of the 1906 earthquake.

within ±40° to capture these obliquely-striking structures. The structure of the fault zone outlined by our analysis agrees well with the mapped location of active faults (Figure 3). An exception to this is the SW margin of Mustang Ridge, where headward incision into the ridge creates a landslide scarp that trends parallel to the SAF. Finally, in the Peninsular Bay Area near Black Mountain, the SAF has a small restraining bend that causes the fault to undergo a transition from a relatively simple, linear fault trace to a progressively bifurcating trace to the NW. Applying a filter identical to that used in the Carrizo Plain, the location of the SAF identified by our analysis closely mimics that mapped independently (Figure 4). Interestingly, the location of the 1906 rupture, which is the most recently active fault strand, is correctly identified as a scarp with the lowest κt value, while flanking traces are characterized by larger κt values.

4. Discussion and Conclusions

[11] This method appears to image the salient characteristics of a fault zone in the areas investigated; however, it suffers from a number of limitations. First, the resolution of the location of scarps varies with morphologic age, and so precise location of a given fault scarp may be difficult to identify using this analysis. Secondly, geomorphic features created by surface processes that mimic elongated scarps will incorrectly be identified as fault scarps. For example, in the Carrizo Plain, multiple channels trending perpendicular to the fault scarp have banks that are falsely identified as fault scarps. Filtering the results for a range of orientations about that of the overall trend of the fault zone ameliorates this problem; nonetheless, our analysis shows that in some cases, these features may still be incorrectly identified as fault scarps. These limitations suggest that such an analysis should be complemented by quality control such as visual inspection, which in most cases can identify those areas in which the algorithm has failed.

[12] Despite these limitations, the method apparently provides a way to quickly and automatically image and characterize the first-order aspects of the fault-zone geomorphology in the trial areas studied. Given the large amount of random and systematic geomorphic noise that obscures the component of topography produced by fault motion, it is remarkable that the location of extracted fault geometries approximately corresponds with those that are mapped, and that systematic patterns in the morphologic age distribution of scarps emerge from the analysis. This results from the linear nature of fault scarps that allows us to use an elongated template that increases the SNR by considering multiple, parallel scarp profiles in the analysis. This suggests that this analysis may be used along the entire length of a fault to produce a coarse view of the spatio-temporal evolution of the fault zone based on the record of recent deformation represented by the fault zone topography.

[13] **Acknowledgments.** GEH acknowledges support from the Terman Fellowship provided by Stanford University. We acknowledge T. Hanks, T. Perron, and an anonymous reviewer for insightful and constructive comments that improved the manuscript.

References

Andrews, D. J., and R. C. Bucknam (1987), Fitting degradation of shoreline scarps by a nonlinear diffusion model, *J. Geophys. Res.*, *92*, 12,857–12,867.

Arrowsmith, J. R., D. D. Rhodes, and D. D. Pollard (1998), Morphologic dating of scarps formed by repeated slip events along the San Andreas Fault, Carrizo Plain, California, *J. Geophys. Res.*, *103*, 10,141–10,160.

Davis, W. M. (1892), The convex profile of bad-land divides, *Science*, *508*, 245.

Gallant, J. C., and M. F. Hutchinson (1997), Scale dependence in terrain analysis, *Math. Comput. Simul.*, *43*, 313–321.

Gilbert, G. K. (1909), The convexity of hillslopes, *J. Geol.*, *17*, 344–351.

Hanks, T. C. (2000), The age of scarplike landforms from diffusion-equation analysis, in *Quaternary Geochronology: Methods and Applications*, edited by J. Stratton Noller, J. M. Sowers, and W. R. Lettis, pp. 313–338, AGU, Washington, D. C.

Hanks, T. C., and D. J. Andrews (1989), Effect of far-field slope on morphologic dating of scarplike landforms, *J. Geophys. Res.*, *94*, 565–573.

Hanks, T. C., R. C. Bucknam, K. R. Lajoie, and R. E. Wallace (1984), Modification of wave-cut and faulting-controlled landforms, *J. Geophys. Res.*, *89*, 5771–5790.

Lawson, A., and H. Reid (1908), *The California Earthquake of April 18, 1906: Report of the State Earthquake Investigation Commission*, Carnegie Inst. of Washington, Washington, D. C.

Rymer, M. J., M. Lisowski, and R. O. Burford (1984), Structural explanation for low creep rates on the San Andreas fault near Monarch Peak, central California, *Bull. Seismol. Soc. Am.*, *74*, 925–931.

Sarna-Wojcicki, A. M., E. H. Pampeyan, and N. T. Hall (1975), Map showing recently active breaks along the San Andreas fault between the central Santa Cruz Mountains and Northern Gablian Range, California, *U.S. Geol. Surv. Misc. Field Stud. Map*, *MF-650*.

Scholz, C. H. (1988), *The Mechanics of Earthquakes and Faulting*, Cambridge Univ. Press, New York.

Vedder, J. G., and R. E. Wallace (1970), Map showing recently active breaks along the San Andreas and related faults between Cholame Valley and Tejon Pass, California, *U.S. Geol. Surv. Misc. Invest. Ser. Map*, *I-574*.

JR. Arrowsmith, School of Earth and Space Exploration, Arizona State University, PO Box 871404, Tempe, AZ 85281, USA.

K. Blisniuk, Department of Geology, University of California, One Shields Rd., Davis, CA 95616, USA.

S. DeLong and C. Prentice, U.S. Geological Survey, Mail Stop 977, 345 Middlefield Rd., Menlo Park, CA 94025, USA.

G. E. Hilley, Department of Geological and Environmental Sciences, Stanford University, Braun Hall, Bldg. 320, Stanford, CA 94305-2115, USA. (hilley@stanford.edu)